Available online at www.sciencedirect.com
ScienceDirect
Journal of the European Ceramic Society 30 (2010) 1277–1286
www.elsevier.com/locate/jeurceramsoc

A consecutive decomposition–sintering dilatometer method to study the effect of limestone impurities on lime microstructure and its water reactivity

D.T. Beruto [a,*], R. Botter [a], R. Cabella [b], A. Lagazzo [a]

[a] DICAT, Faculty of Engineering, University of Genoa, Piazzale. J.F. Kennedy, Pad. D, 16129 Genoa, Italy
[b] DIPTERIS, Faculty of Science M.F.N., University of Genoa, Corso Europa 26, 16132 Genoa, Italy

Received 27 July 2009; received in revised form 17 November 2009; accepted 18 December 2009
Available online 13 January 2010

Abstract

In this paper we develop a consecutive decomposition–sintering dilatometer method (CDSD) to study the effect of limestone impurities on lime microstructure features that are formed during the limestone decomposition. Two experimental parameters, the changing in slope of the dilatometer traces ($\dot{\beta}$) and the total shrinkage of the produced lime (Σ) in the subsequent sintering stage, have been shown to be influenced by the impurities. The first limestone investigated was poorly recrystallized with heteroblastic texture and a total amount of impurities equal to 2.2 wt%. The second limestone was strongly recrystallized limestone with equigranular xenotopic fabric and with 0.7 wt% total impurities. $\dot{\beta}$ and Σ turns-out to be 13×10^{-4} [min^{-1}] and 1.43 wt% for the lime from the first sample, and 3×10^{-4} [min^{-1}] and 11.2 wt% for the calcium oxide from the second one. Sintering steps among CaO grains catalysed by the escaping CO_2 lead, in the first lime–limestone matrix, to lime grains of irregular shapes and average dimensions between 3 and 7 μm. In the second lime–limestone matrix, liquid phases between CaO and impurities promote locally denser oxides regions mixed with others where solid-state sintering steps occurs. In these regions the average grain dimensions are 6–10 μm. CDSD methods allow to understand the lime water-reactivity vs. the temperature of lime formation tests in term of competition between coarsening and densification phenomena occurring in the temperature range 700–1200 °C and in air.

Keywords: Sintering; Thermal expansion; Calcination; CaO; Dilatometry

1. Introduction

Although the endothermic decomposition of calcium carbonate to yield calcium oxide and carbon dioxide has been studied for considerable time by many researchers,[1–11] it is still difficult to apply the extensive valuable scientific knowledge obtained to the complex phenomena that occur during limestone decomposition processes.

Part of the difficulty stems from the complex nature of limestone. For instance, the presence of biosparites, of different grain sizes of calcium carbonate crystals and different types of impurities change the textural and mineralogical properties of limestone even at the single-quarry scale, as shown by the analyses resulting from different laboratories. Obtaining a general view of the effects of these variables on the mechanisms of formation and textural evolution of the lime grains is a difficult task.

Pioneering and previous studies[12–14] have shown that the sintering of CaO grains from $CaCO_3$ is catalyzed by the activity of the CO_2 escaping from the reaction interface zones. The evolution of the CaO porosity and of its surface area, drop suddenly when the CO_2 partial pressure is average 9 Torr at the temperature of 650 °C.[15] Since the value of the CO_2 partial pressure inside the block-like limestone decomposing in air is very reasonably higher than the threshold value required to drop the oxide specific surface area, the obtained lime should have low surface area independently from the nature of the limestone. The experimental data[5] are in agreement with this prediction. Indeed the surface area values of many lime obtained from different sources of limestone in industrial furnaces are included in the range of few square meters, but shape, size of the lime grains and porosity of agglomerates can be very different. Evidently the limestone impurities of the different samples, play an important role in the formation of the correspondent lime microstructure.

In this paper we wish to address this topic. It is well known[16] that the addition of simple salts to calcium carbonate powders accelerates the decomposition of the carbonate and changes

* Corresponding author. Tel.: +39 0103536039; fax: +39 0103536034.
E-mail address: dabe@unige.it (D.T. Beruto).

0955-2219/$ – see front matter © 2010 Elsevier Ltd. All rights reserved.
doi:10.1016/j.jeurceramsoc.2009.12.012

the shape and the size of the calcium oxide grains through the action of low eutectic melting phases. However, before applying these mechanisms to the decomposition of block-like limestone samples it is necessary to obtain information on the limestone impurities, whose nature and distribution inside the limestone matrix is a consequence of the genetic environment and of diagenetic processes of the different limestones.[17] Quite often the impurities are not formed by simple salts and they are randomly distributed and selectively concentrated in stilolites and/or veins reaching a local high concentration even if the bulk $CaCO_3$ concentration is around 99 wt%.

Thus, during the decomposition of a given sample, liquid phases can be active near the impurity islands, while solid–solid and/or solid–gas steps can be important in other regions. As the bulk $CaCO_3$ concentration of most limestones is near 99%, it is possible that the global kinetics of the thermal decomposition are almost unchanged throughout the limestone, but final lime microstructural and textural properties are not.

If this is so, the traditional TG, XRD and SEM analyses are not enough to investigate these kinds of phenomena. In this paper, in order to obtain data on the length-variation of block-like limestone due to its decomposition reaction and to changes in the lime microstructure within it, we will present and discuss a new consecutive decomposition–sintering dilatometer method. Since the decomposition and the sintering stages are carried-out on the same block-like sample without removing it from the furnace, it will be shown that the effect of the impurities on the sintering rate of the lime is an "*enlarged*" picture of the complex phenomena of the lime microstructure changes during the limestone thermal decomposition stage.

As a technological and scientific consequence of these findings we can explain why the hydration kinetics involving the calcium oxides and liquid water yields significant differences and unexpected results.

2. Materials and experimental methods

2.1. Mineralogical and textural analysis of limestone

Table 1 shows the two kinds of limestone used throughout this work (A and B) both characterized by a high $CaCO_3$, 97.79% for sample A and 99.34% for sample B. The same table includes the concentration of elements and the impurities in the carbonate matrix, derived from spectroscopic analysis.

The specimens, taken from large block sample, were prepared for the thin section (30 μm in thickness) analysis under a polarizing microscope. Stereomicrograph pictures were taken to obtain textural features at a large scale while polarized light micrographs under crossed polar were taken to obtain the texture at a smaller scale.

SEM-EDS images and qualitative spectra of the mineral phases were made on carbon-coated polished thin sections with a Philips SEM 515 equipped with an energy-dispersive spectrometer (EDAX PV9100).

To clearly visualize the textural features and accessory mineral location of sample B, an acid etching method was used as follows: the polished sample was etched with 2.5% acetic acid for 30 s, then carefully rinsed with distilled water and dried (24 h at 60 °C) and finally carbon-coated for SEM analyses.

2.2. Thermogravimetric and dilatometric analysis

A large, representative block of limestone was cut following the compositional layering broadly marked by dark minerals as reference plane (more evident in sample A), visually checked. The B samples were cut into 10 cm × 10 cm × 10 cm cubes and the A samples into slices of 1.2 cm in thickness and irregular shape with an area of about 400 cm^2. These blocks were drilled perpendicularly to the reference plane using water-cooled diamond-core drill bits to obtain cylinders of 6 mm in diameter and 12 mm or more in thickness. Some samples were also drilled parallel to the reference plane to check the influence of a different direction on the thermal behaviour.

All samples were successively divided into pieces 3 mm in height to obtain specimens from the same sources to duplicate the runs with the TG, DSC and dilatometer. The limestone samples used to characterize the porosity features were cylinders 12 mm in height, selected from the same source.

The TG experiments were carried-out in a static air atmosphere using a Netztch STA 409. TG-DSC thermal analyzer in the sensitivity range of ±0.1 mg equipped with a Netztch 410 furnace temperature controller system. For each run the samples were placed inside the furnace on a 6 mm diameter TG-DSC sample alumina holder and then the temperature was first raised from room temperature (about 20 ± 1 °C) to 1200 °C at a nominal rate of 10 °C/min and the weight loss recorded continuously. At the end of the decomposition the furnace temperature was cooled down at the same nominal rate of 10 °C/min of the heating period. The previously prepared calcium oxide bodies were stored in sealed vials with a silica gel desiccator for a few hours. The oxide fracture surfaces were successively sputtered with a gold layer of about 200 nm for SEM observation.

Consecutive decomposition–sintering dilatometer experiments were carried-out in a Netzch dilatomer (DIL 402 E) equipped with a furnace identical to the one used in the TG runs and controlled by the same systems. The internal diameter of the DIL 402 E furnace was 26.5 mm, equal to that of the vertical TG-DSC furnace. The pushing-rod was 6 mm diameter alumina with an added applied force of 0.3 N

Table 1
Mean chemical composition of A and B limestone obtained from a representative quarry sample.

Sample	$CaCO_3$ (%)	MgO (%)	SiO_2 (%)	Al_2O_3 (%)	S (%)	Fe_2O_3 (%)	MnO (%)	Na_2O (%)	K_2O (%)	SrO (%)	P_2O_5 (%)	Cl (%)	F (%)
A	97.79	0.55	0.58	0.14	0.033	0.062	0.0017	0.0047	0.041	0.144	0.10	0.0052	0.03
B	99.34	0.15	0.05	0.01	0.005	0.029	0.0245	0.0021	0.002	0.124	0.06	0.0052	0.054

Limestone cylinders (6 mm in diameter and 3 mm in length) from the same sample of those placed in the thermobalance, were introduced into the dilatometer and heated in static air using the same heating program adopted for the TG experiments. Each run was duplicated with fresh samples to evaluate any statistical deviation. TG traces turned out to be reproducible within the instrumental error of 2%, while the dilatometer ones between the 2% and the 4%.

Longitudinal shrinkage was recorded continuously, while the radial shrinkage was checked at room at the end of the experiments temperature with a micrometer (the accuracy was of ±0.01 mm). It was noted that the total radial and longitudinal shrinkages were fairly equal within the experimental errors.

Blank runs to calibrate the thermal expansion of the sample holder were done using polycrystalline alumina furnished by NETZSCH.

From other runs[18] we were aware that the thermal dilation period before the decomposition stage can depend on the drilling direction. A number of tests on limestones showed that in some cases a difference of about 2–4% can be observed between the parallel and the perpendicular drilling directions. However these differences do not change the slope of the traces in the subsequent decomposition and sintering stages.

Lime isothermal sintering experiments were performed to understand the water-reactivity test of the CaO. These samples were prepared with the following thermal heating program: (1) heating to 670 °C at 10 °C/min and kept at this temperature for 25 min. (2) Raising the temperature of the selected sintering temperature at 50 °C/min (by the time the limestone reaches the sintering temperature, it has completed its decomposition). (3) Keeping the sample at that temperature for 150 min for the sintering stages. (4) Cooling to room temperature at 10 °C/min. (5) Checking of the sample geometry. For these runs the sample holder correction table furnished by Netzsch was used.

Mercury porosimetry characterisations were done by using a porosimeter model *Carlo Erba* 2000. To reduce moisture hydration, the samples were placed in the porosimeter sample holder (dilatometer), under mechanical vacuum conditions (≈10 Pa) within a few minutes. After 20 min of degassing Hg was introduced into the dilatometer and the pressure was increased up to 750 bar. Blank runs were done using the same dilatometer filled only with Hg. All the runs were done at the room temperature. Hysteresis loops were observed for all samples, but for this paper, being our main interest the one obtaining data for the total open porosity, we report only the intrusion curves. Analysed samples were CaO lime cylinders of about 6 mm in diameter and 12 mm in length.

SEM images were taken of the fracture surfaces of the limes produced with the consecutive decomposition–sintering method in various temperature-heating programs.

2.3. Water-lime reactivity

Defined quantities of water and fine lime powders were mixed with a mechanical stirrer in a thermally insulated Dewar flask, and the reaction temperature was monitored. Accordingly to the Standard DIN 1060 part 3 method,[19,20] the time t_{60} required to reach the reaction temperature of 60 °C was measured for the different limes obtained from the same limestone samples (A and B) decomposed in air at different temperatures for given retention times. This parameter was taken to indicate the water-lime reactivity.

3. Results and discussions

3.1. Limestone texture and impurities

The macroscopic textural features of samples A and B show that irregular micrometric veins are present in the A matrix, while coarser crystal grains characterize the B sample. The textural features are shown in Fig. 1. Images 1 and 3 show that sample A is formed of a nearly-pure fine-grained crystalline limestone (slightly recrystallised) with a heteroblastic texture. Some traces of allochemical components (fragments of fossils) are visible in the thin section. Unfortunately the original abundance of these allochems cannot be determined as a consequence of recrystallisation that affected this limestone. The presence of scattered sparry calcite crystals (up to 0.5 mm in size), could also be related to the recrystallisation processes. The sample shows layering marked by the presence of some dark submillimetric stilolitic layers rich in opaque minerals. Some (rare) idiomorphic millimetric plagioclase crystals have been found. Except for some sparry calcite individuals, the calcite crystals are anhedral and range in size between 1 and 15 μm.

Images 2 and 4 show that sample B is a nearly-pure fine-grained strongly recrystallised limestone with an equigranular xenotopic fabric.[17,21] The mean grain size of the carbonate crystals is between 50 and 75 μm. There are some microcrystals (up to 5 μm in size) of opaque minerals, mainly as scattered grains irregularly distributed. There are also rare calcite microveins (up to 0.25 mm in thickness).

The SEM-EDS analysis was focused on identifying the composition and location of the carbonate and accessory minerals in both samples.

As images 1, 3 and 5 in Fig. 2 show, in the sample A the carbonates are formed of nearly-pure calcite (Mg, Sr and other elements, if present, are in trace amounts). Some very rare anhedral irregular patches of dolomite have been found, possibly related to secondary dolomitisation processes in the stilolites. The occurrence of accessory minerals is related to the presence of stilolites where (in order of decreasing abundance) apatite, pyrite, plagioclase and quartz are found. Apatite is present as micrometric crystal aggregates; pyrite is present both as micrometric euhedral crystals and framboidal aggregates. The SEM-EDS spectra revealed that the plagioclase is pure albite; the apatite spectra revealed a lack of appreciable amounts of fluorine and chlorine.

Images 2, 4, and 6 in Fig. 2 illustrate the results for sample B.

Carbonates are represented by nearly-pure calcite, as in sample A. The etched-sample study revealed that accessory phases are present both as intergranular and inclusion minerals (Figs. 2–6). There are also Quartz, apatite, K–Al rich phyllosilicates and rare fluorite (in order of decreasing abundance). The SEM-EDS spectra revealed the presence of fluorine in apprecia-

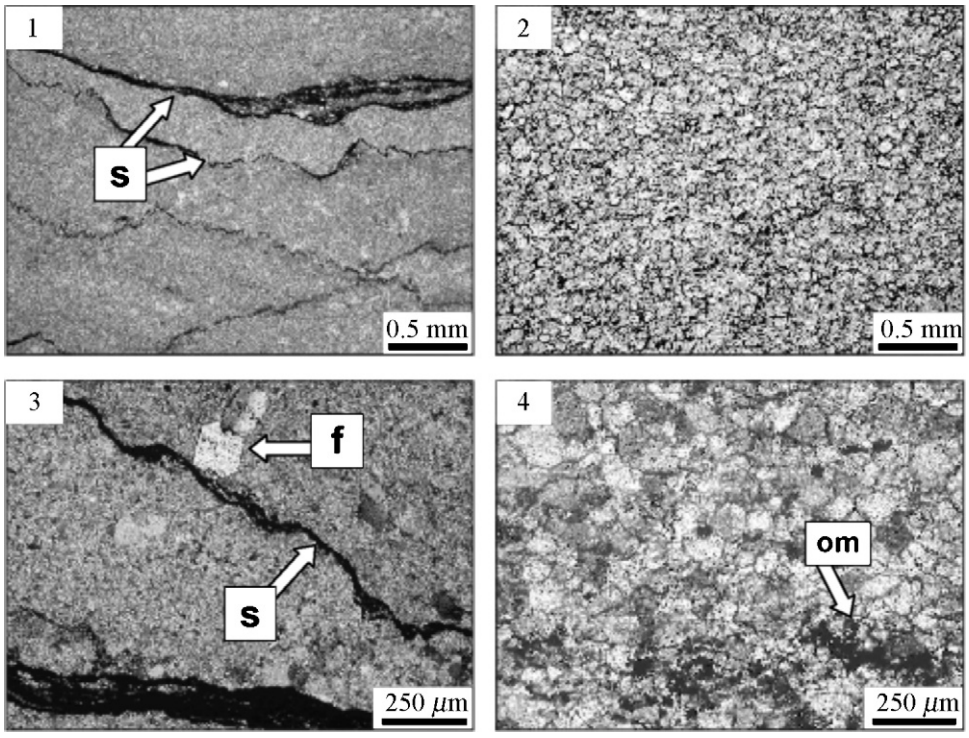

Fig. 1. Polarized light (under crossed polars) micrographs. Photos 1 and 3: sample A; photos 2 and 4: sample B. Photo 1 shows the presence of opaque minerals in stilolites; photo 2 evidence the coarser texture of sample B; in the photo 3 the rare feldspars occurring as accessory minerals in sample A show their idiomorphic habitus. Photo 4 shows the occurrence of opaque minerals as microcrystalline irregular aggregates in sample B. S, stilolites; f, feldspar; om, opaque minerals

ble amounts also in the apatite. A comparison of the F contents of samples A and B revealed that this element is selectively concentrated in Fluorite and apatite only in sample B. The lack of both fluorite and F in the apatite EDS spectra of sample A could be explained by a lower F content and lower recrystallisation; in sample B the genesis of the fluorite and the incorporation of fluorine in the apatite could be related to mobilization processes during recrystallisation.

As low eutectic melting phases have been observed in the system, calcite–calcium oxides with fluorine and chlorine compounds such as LiF[22] and LiCl,[23] it can be inferred that some liquid phases played a role in the formation of the lime microstructure during the decomposition of limestone B because the apatite spectrum of this sample is richer in fluorine than that of limestone A.

3.2. Decomposition–sintering processes

Fig. 3 shows reproducible and typical dynamic TG traces involving the thermal decomposition of compact bodies in limestones A and B under the same conditions.

It is possible to note that the traces are quite reproducible and their total apparent activation enthalpy can be derived through the usual kinetic analysis of non-isothermal rate measurements.[24] For our derivation we selected the general equation that reads:

$$\ln\left(\frac{d\alpha/dt}{f'(\alpha)}\right) = \ln\left(\frac{A}{b}\right) - \frac{\Delta H*}{RT} \quad (1)$$

where α is the degree of advancement of the reaction, $f'(\alpha)$ the differential form of $\alpha(t)$ which best fits the experimental data from 0 to 1, T the absolute temperature, A the constant which includes the entropy and frequency terms, ΔH^* the total apparent activation enthalpy and R the gas constant.

Usually, non-isothermal kinetic analyses are performed using multi-heating rate TG methods.[25–27] Experiments based on different heating rates[28–30] have the advantage of not requiring any assumption on the shape $f'(\alpha)$ vs. time function, while those obtained from a single heating rate do.

The number of differential, integral and non-isothermal forms of kinetic expressions are numerous.[24,27] In our experiments the limestone samples 6 mm in diameter and 3 mm in height were kept in an alumina crucible of equal diameter. It is reasonable to assume that the sample starts to decompose from all three external surfaces, but in the close space that surrounds the lateral and the bottom surfaces, the CO_2 pressure value might be near to the equilibrium one. If so, the predicted advance of the interface would occur mostly from the top-down direction as happens in the decomposition of single large calcite crystals in a Langmuir cell.[1] Thus, under the assumption that the heat transport rates are not the rate determining step, as first attempt to derive value for the total apparent enthalpy of activation, it is possible to use the kinetic expression based on geometrical models, which reads.[31,32]

$$1 - (1 - \alpha)^{1/n} = Kt \quad (2)$$

n being a number equal to 1 for the linear advance interface, equal to 2 for the contracting area equation and equal to 3 for the contracting volume mechanisms.

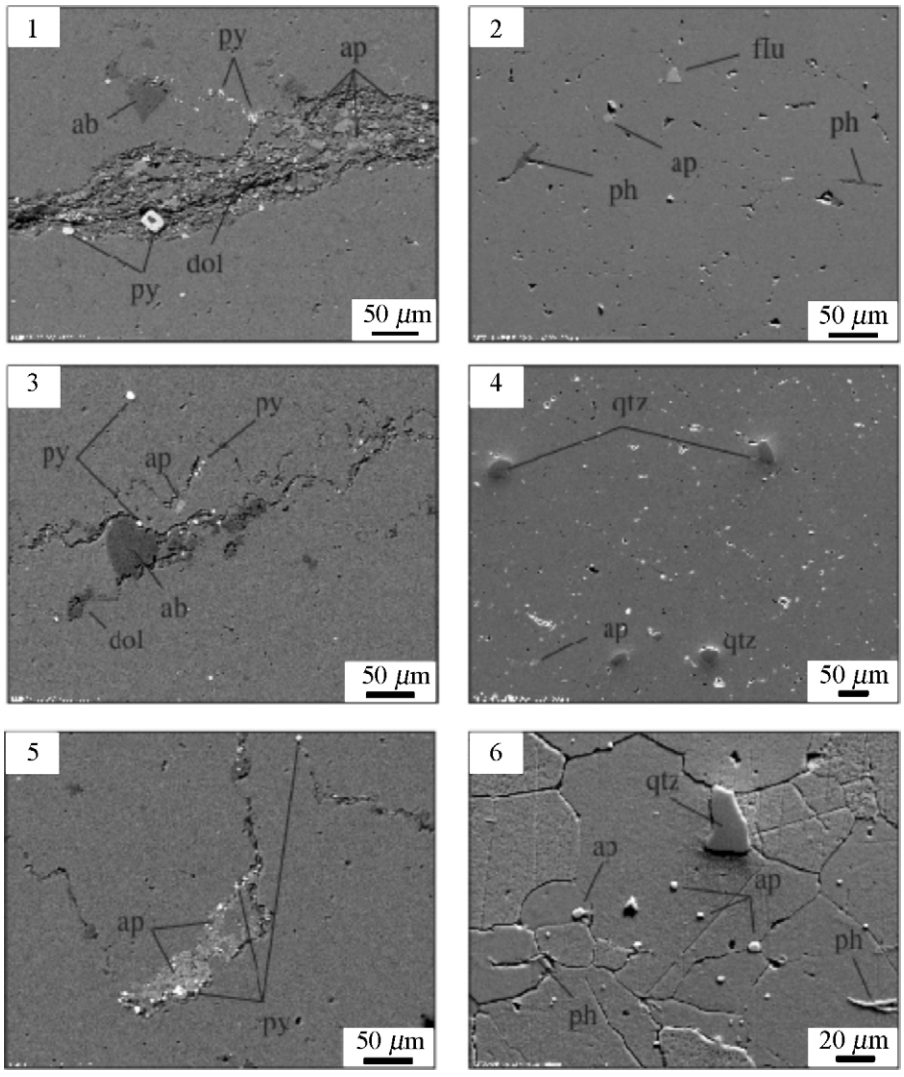

Fig. 2. SEM-BSE images. Images 1, 3 and 5: sample A; images 2, 4 and 6: sample B. The medium grey background is calcite. Images 1, 3, and 5 show the accessory mineral occurrences in sample A: apatite (light grey) occurs in cryptocrystalline aggregates of idiomorphic crystals selectively concentrated together with pyrite (white) and rare crystals of albite (dark grey) in the stilolites; dolomite rarely occurs in irregular xenomorphic grains (arrowed in image 3). In sample B the occurrence of accessory minerals is mainly represented by scattered micrometric crystals of apatite (fluorine-rich), pyrite (not visible in the selected images), rarer phillosilicate (K–Al rich) lamellar grains and some quartz grains. Occasionally idiomorphic fluorite crystals occur (image 2). Image 6 represents the same sample after the chemical etching with acetic acid solution: the textural features of the calcite grains are highlighted and the occurrence of accessory phases both as inclusions and intergranular phases is evident. Abbreviations: ab, albite; ap, apatite; dol, dolomite; flu, fluorite; ph, phyllosilicate; py, pyrite; qtz, quartz.

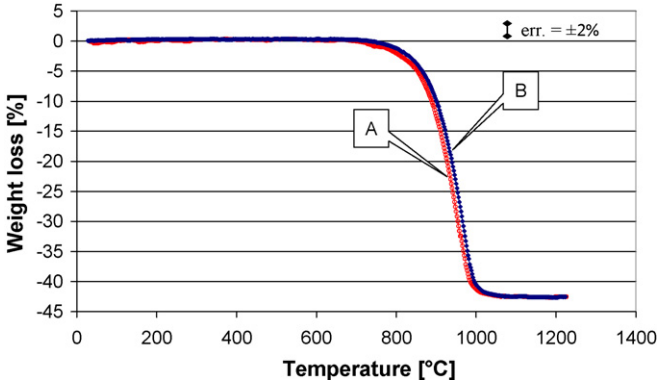

Fig. 3. TG traces obtained by heating the compact A and B limestone bodies at a heating rate of 10 °C/min in air.

Assuming $n = 1$, this equation fits our experimental data in the range of α between the 0 and 0.7

The values of the total apparent enthalpies of the reaction from the logarithmic plot of Eq. (2) are equal to 160 ± 0.6 kJ/mol for sample A and 175 ± 0.5 kJ/mol for sample B respectively (correlation for both $R^2 = 0.998$)

These results clearly show that the effects of small amounts of impurities on the lime microstructure formed in the 99% calcium carbonate matrix, are not detectable from TG experiments although the corresponding kinetic analysis leads to slightly different total apparent enthalpies of activation.

To obtain a thermal method which is more sensible to the presence of impurities, let us discuss the following consecutive decomposition–sintering approach.

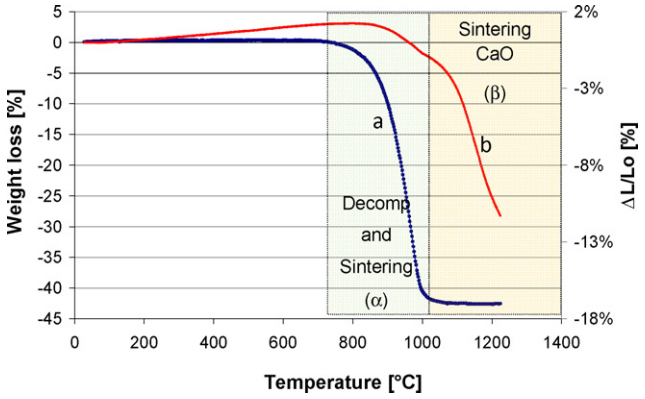

Fig. 4. Comparison of thermogravimetric (a) and dilatometric traces (b) of two identical samples of limestone B obtained from TG and dilatometer analysis carried-out under the same conditions.

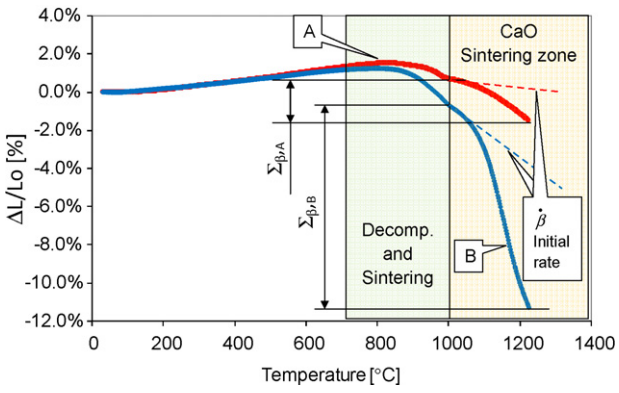

Fig. 5. Comparison of the dilatometer decomposition–sintering curves of the two different limestones, A and B, whose mineralogical properties and impurity distribution have been proved to be different, but have almost equal TG traces (see section above and Fig. 4).

Fig. 4 compares the thermogravimetric (a) and the dilatometric traces (b) of two identical samples of B limestone obtained respectively from TG and dilatometer analyses carried-out under identical conditions. As can be noted the dilatometric trace can be divided into three different regions.

In the region λ, where the TG curves do not give weight variation, the sample length increases due to the limestone thermal expansion.

In the region α, which starts when the TG curve shows that the decomposition reaction is beginning, a number of complex thermal steps occur. The limestone decomposes, the CO_2 diffuses through the formed CaO grains promoting their sintering,[15] the limestone impurities can interact with both the $CaCO_3$ and CaO or with only one of the solid phases. The actual sample length in this region will be a balance between different contributions. Thermal dilatation of $CaCO_3$ and CaO will tend to increase the sample length, while the reduction in the molar volume due to the limestone–lime reaction and the sintering of the oxide formed will decrease it. Fig. 4 shows that at a certain degree in the advancement of the decomposition reaction, the reduction in length prevails.

Let us call $\Sigma_\alpha = \Delta L/L_0$ the total longitudinal shrinkage due to the all thermal phenomena occurring in region α.

In the region β which starts when the thermal decomposition of the limestone is complete, the dilatometer traces can be ascribed only to thermal phenomena inside the matrix of the formed CaO grains. Among these phenomena are sintering, grain size growth, porosity reduction, interactions with impurities, which might lead to liquid phases.

It is interesting to note that the dilatometer decomposition–sintering curve changes its slope at the β starting temperature.

Let us call $\Sigma_\beta = \Delta L/L_0$ the global shrinkage associated with this region.

It is known[33,34] that the sintering rates of porous ceramic oxide bodies are strongly dependent on the green density of the starting-grain oxide-packing body. Since the lime "green bodies" have been formed "*in situ*" from the decomposing limestone and have not been removed from the furnace, the initial sintering rate ($\dot{\beta}$), as well as the total shrinkage Σ_β, must be strongly dependent on the microstructure of the lime formed during the limestone decomposition.

So, if the limestone impurities are able to change the microstructure of the limes obtained this effect should be enhanced in the region β, which only involves the sintering of the lime produced at high temperature.

Fig. 5 compares the dilatometer decomposition–sintering curves of the two different limestones A and B, whose mineralogical properties and impurities distribution have been proved to be different, but that have almost identical TG traces (see above section and Fig. 3). It can be noted that while the TG traces are almost equal/identical, the corresponding dilatometric curves are very different.

Table 2 lists the values of $\dot{\beta}$ and Σ_β obtained from the β regions of Fig. 5.

Since the comparison is done for limestone samples of equal geometry heated under the same conditions, the difference in the corresponding Σ_β and $\dot{\beta}$ clearly indicate different interactions between the CaO oxides and the impurities.

In particular, since $\dot{\beta}_B$ and $\Sigma_{\beta,B}$ are greater than $\dot{\beta}_A$ and $\Sigma_{\beta,A}$, *A* the matter transport should occur at a faster rate inside the B lime matrix than inside the A one.

Fig. 6 illustrates two images (A and B) of SEM observations of fractured surfaces of limes A and B obtained at 1200 °C in air after equal/identical decomposition–sintering processes and then cooled to room temperature.

The average CaO grains size of lime A (3–7 μm) is smaller than that of lime B (6–10 μm), but a greater difference is that the B grains are forming two set of aggregates; the first one with grain shape and spatial arrangements near that observable in

Table 2
Values of $\dot{\beta}$ and Σ_β obtained from the CaO sintering zone in Fig. 5.

Sample	Initial sintering rate ($\dot{\beta}$) ($\Delta L/L_0$, min)	Total shrinkage (β period) ($\Delta L/L_0$, %)
A	0.0003	1.43
B	0.0013	11.2

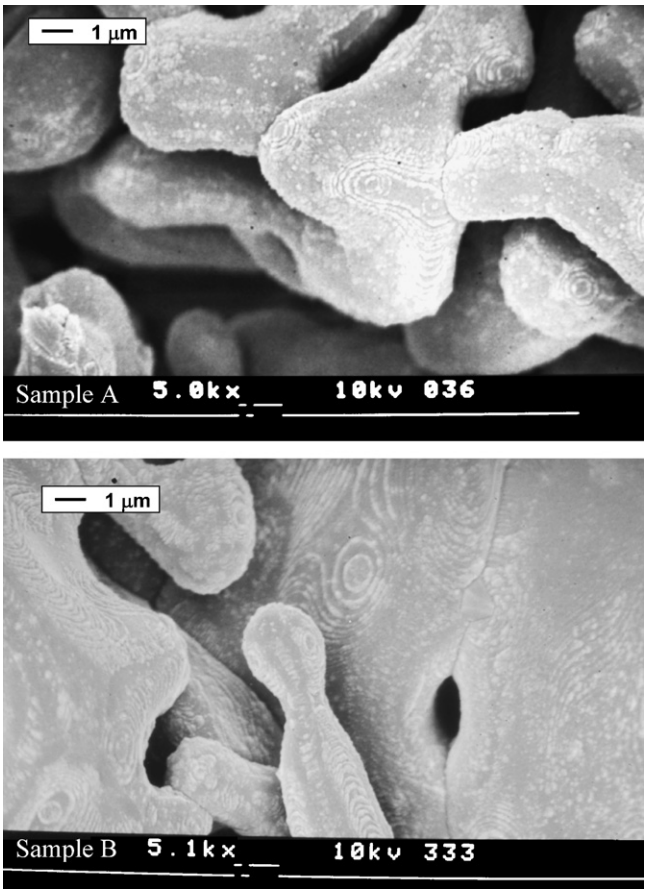

Fig. 6. Typical SEM observations on fractured surfaces of lime A and lime B obtained through the same decomposition–sintering process: 1200 °C for 150 min.

the A oxide, the second one formed by a denser microstructure where some liquid phase was probably operating. The denser aggregates do not form a continuous network but are separated by large macropores.

In agreement with our previous data[10] the first kinds of CaO aggregates look like those often observed when CaO grains undergo a solid–solid sintering process catalysed by the escaping CO_2. The second one suggests the presence of a surface liquid phase where the CaO can be dissolved and recrystallised.[35,36]

On both CaO surfaces (A and B grains) interesting patterns, which look like Moire fringes, appear, but at present we cannot be sure about their formation. It may be that these patterns are the result of low-temperature reactivity between edge the CaO facets and air moisture after the fracture of the sample. However, we cannot exclude the possibility that they are the results of high-temperature vaporization–condensation process of some volatile impurities.

The total shrinkage $\Sigma_{\beta,A}$ is less than $\Sigma_{\beta,B}$. This result cannot be easily explained because many complex phenomena can happen simultaneously. While $\Sigma_{\beta,B}$, is due to terms that can be accounted for by a locally-formed liquid phase and by solid-state transport phenomena $\Sigma_{\beta,A}$ should be mainly due to matter transport process in the solid phase.

As a matter of discussion it is interesting to observe the values, $\dot{\beta}_A$ and $\dot{\beta}_B$, of the initial lime sintering rates. As Table 2 is showing $\dot{\beta}_B$ is greater than $\dot{\beta}_A$. This datum seems to indicate that the B grain size is smaller than that of the A-lime.[37]

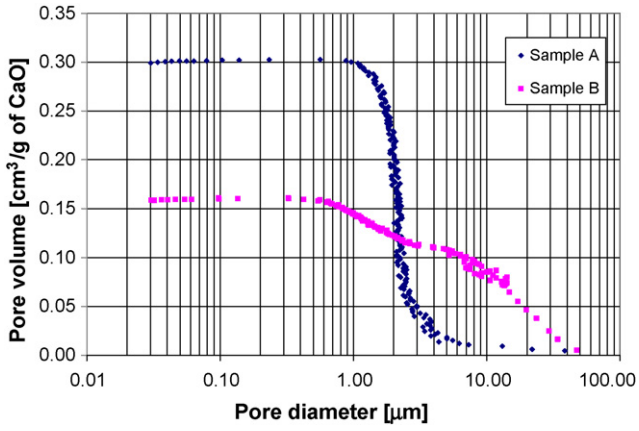

Fig. 7. Hg intrusion curves of the lime A and B produced using the thermal treatment of Fig. 8 at sintering temperature of 1190 °C.

But as it has been observed previously (see also Fig. 1 of supplementary material) the B particles have an average dimensions greater than the A ones. Evidently the initial lime sintering rate is dependent upon other microstructure variables.[38] The dilatometer technique allows to record the total length of the samples, which at the beginning of the sintering step is strongly connected with the spatial arrangements of the lime particles within a fixed total volume. Thus this parameter is connected with the packing of the lime grains inside this volume at the start-up of the sintering step. Comparison between the data concerning samples A and B, assuming almost isotropic shrinkage, allows to say that the A porous body is greater than the 4% of the B one. In other words smaller particles in A porous body are less packed than bigger grains in B body. Due to this the A initial global sintering rate is less than the B one.[38]

Hg porosimeter analysis, carried on the final sintered lime (see Fig. 7) nicely confirm that the packing of sample B is greater than the packing of sample A. Indeed the Hg-porosity of sample B is 0.15 cm^3/g, while the one of sample A is 0.30 cm^3/g. On this basis it is possible to obtain information on the evolution of the lime microstructure during the sintering through analysis of the microstructure on the final sintered lime.

SEM-EDS spectra (see section above) show a lack of F-bearing phases in appreciable amounts in limestone A, while in limestone B the fluorine is partitioned into fluorite (CaF_2) and apatite. These spectra suggest that the fluorine mobilisation and reconcentration processes took place during recrystallisation. Islands of impurities are located around well crystallised calcium carbonate grains in limestone B. It may be that the B lime microstructure is due to an initial nucleation and growth of CaO grains due to the adsorption and desorption of CO_2 from the CaO surfaces and by the penetration of some CO_2 molecules inside the CaO bulk lattice.[14] But those CaO grains formed near to rich fluorine regions might subsequently give phases that are liquid at the sintering temperature. These phases flow to a certain distance, dissolve some CaO through patterns that give the denser oxide zones as their final result.

Table 3
Relationship between t_{60} and decomposition temperature for limes A and B.

Sample	T_{decomp} (°C)	t_{60} (s)	$1/t_{60} \propto \langle r_{60} \rangle$ ($\times 10^3$ s^{-1})
A	980	22	45.45
	1060	44	22.72
	1140	108	9.26
	1200	195	5.13
B	980	280	3.57
	1060	1105	0.90
	1140	1428	0.70
	1200	1091	0.91

Table 3 reports the t_{60} water-lime reactivity of each type of lime obtained from the decomposing of the parent limestone at fixed temperature T_d in air. In the same table (column 4) an average lime dissolution rate, $\langle r_{60} \rangle \propto 1/t_{60}$ is reported for the sake of comparison.

The data provide two interesting results that require an explanation. The first suggests that the water-lime reactivity rate in sample A is always faster than that in sample B, no matter what the decomposition temperature T_d at which the parent limestones decomposed. In general, the water-lime reactivity rate is controlled by the lime microstructure and by the surface chemical composition of the calcium oxide grains.[39] By assuming an identical surface reactivity, the lime B grain size should be greater than that of the A samples. This inference is confirmed by the SEM analysis carried-out on lime A and lime B obtained from the decomposition of the parent limestone at 1200 °C.

The second datum shows that the B water-reactivity rate passes through a maximum when the limestone decomposition temperature varies between 980 and 1200 °C. This is a rather surprising result, because t_{60} increases with the decomposition temperature due to the fact that sintering phenomena are more enhanced at a high temperature. While sample A obeys this tendency, lime B does not.

In seeking to understand this datum we applied the consecutive decomposition–sintering dilatometer procedure to three identical bodies of B limestone totally decomposed according to the temperature programme reported in the experimental section, and then sintered isothermally at the temperatures of 1190, 1119 and 1038 °C, i.e. in the temperature range where sample B shows the anomalous water-reactivity behaviour.

Fig. 8 shows the dilatometer traces obtained. It can be noted that Σ_{1038} is less than Σ_{1119}. This is an expected result since the CaO grain size increases with the sintering temperature. However, surprisingly, the shrinkage at 1119 °C equals that at 1190 °C. Evidently the anomalous behaviour t_{60} vs. T_d plots for the B lime is due to new microstructure patterns in that temperature range.

Fig. 9 illustrates the Hg intrusion curves of the three lime samples above. In agreement with image B reported in Fig. 6, the B lime is characterised by a double set of pores, the macrocavities included in the 20-μm dimension and a second class of pores in the region 0.3–2 μm.[40]

At the 1119 °C sintering temperature the total porosity equal to the value found at 1190 °C and Σ_{1119} equals Σ_{1190}, but the

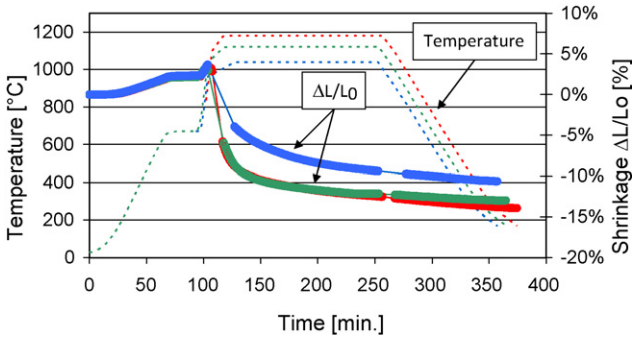

Fig. 8. Dilatometer traces of three equal bodies of limestone B pre-heated to 900 °C and then completely decomposed before the segment at constant temperature (130 min). 60% of the sintering occurs during the heating and 40% occurs isothermally at the temperatures of 1190, 1119 and 1038 °C.

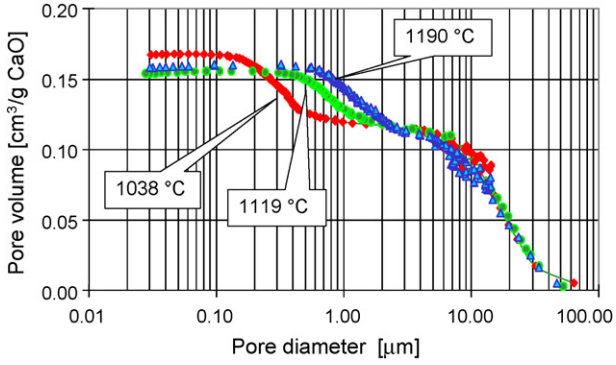

Fig. 9. Hg intrusion curves of the three samples of lime B, produced using the thermal treatment reported in Fig. 8.

micropore distribution is pushed towards larger dimensions. At 1119 °C the average Hg intrusion section is 0.7 μm, while at 1190 °C it is 1.5 μm.

No variations were observed for the macrocavity regions. If the microstructure evolution of the B lime was enhanced locally by the action of liquid phases, this datum strongly suggest that coarsening phenomena can happen, competing with the sintering. On these grounds the temperature T_d at which the curve t_{60} vs. T_d shows a maximum can be considered as the decomposition temperature where the effect of localised impurities form liquid phases with the CaO and promote coarsening over grain densification.

4. Conclusions

In this paper it has been shown that the comparison of the thermal decomposition of block-like limestone samples in a dynamic temperature regime and in air leads to results that are difficult to distinguish, due to the fact that in both sample the $CaCO_3$ content is around 99%. Kinetic analysis of the thermogravimetric traces showed total apparent activation enthalpy values slightly different from and equal to 160 and 175 kJ/mol, but these data "per se" cannot account for the different mechanisms that control the evolution of the lime microstructure.

In this paper we have endeavoured to develop a thermal analysis method that can distinguish differences in the decomposition

rates of limestones and the sintering of the limes obtained from the decomposition.

Using a consecutive decomposition–sintering dilatometer method (CDSD) we have shown that impurities play a major role in changing the kinetics of the decomposition and the subsequent sintering of the limes produced. The experimental parameters that allowed us to measure these effects were the change in slope $\dot{\beta}$ of the dilatometer trace at the end of the decomposition step and the total shrinkage Σ_β measured during the subsequent CaO sintering step.

A comparison of these parameters for the limestone samples investigated here, coupled with the SEM observations, led us to conclude that the lime microstructure evolution during the decomposition process occurs through solid–solid sintering steps and through liquid-assisted sintering ones. The nature and the distribution of the impurities due to the genetic environment and diagenetic processes of the different limestone are responsible for these different microstructure patterns.

The method described here was also able to link the complex lime microstructure evolution with its water-reactivity test. The competition between the coarsening phenomena, due to the effect of the liquid phase, and the sintering step, catalysed by the escaping CO_2, are the two main steps that influence the lime microstructure when impurities form low eutectic melting phases with calcium carbonate and/or calcium oxide. The anomalies observed in the reactivity of one lime and the water have been discussed and explained from the experimental data given by the CDSD method coupled with Hg porosimeter analysis.

Acknowledgements

The authors wish to thank the University of Genoa and the Lhoist Society for their interest in this field of research and L. Negretti (DIPTERIS) for technical help in the mineralogical analysis.

The comments and suggestions made by the students attending the seminars held on this subject at the Faculty of Engineering were of great use.

Appendix A. Supplementary data

Supplementary data associated with this article can be found, in the online version, at doi:10.1016/j.jeurceramsoc.2009.12.012.

References

1. Beruto DT, Searcy AW. Use of the Langmuir method for the kinetic studies of decomposition reaction: calcite. *Journal of the Chemical Society, Faraday Transactions* 1974;**70**:2145.
2. Beruto DT, Searcy AW. Calcium oxides of high reactivity. *Nature* 1976;**263**:221–2.
3. Boyton RS. *Chemistry and technology of lime and limestone*. 2nd ed. New York: Wiley-Interscience; 1980.
4. Powell EK, Searcy AW. Surface-areas and morphologies of CaO produced by decomposition of large $CaCO_3$ crystal in vacuum. *Journal of the American Ceramic Society* 1982;**65**:c42–4.
5. Borgwardt RH. Calcination kinetics and surface area of dispersed limestone particles. *AIChE Journal* 1985;**31**:103–10.
6. Fuller EL, Yoos TR. Surface properties of limestones and their calcination products. *Langmuir* 1987;**3**:753–60.
7. Borgwardt RH. Calcium oxide sintering in atmosphere containing water and carbon dioxide. *Industrial Engineering Chemistry Research* 1989;**28**:493–500.
8. Criado JM, Ortega A. A study of the influence of particle size on the thermal decomposition of $CaCO_3$ by means of constant rate thermal analysis. *Thermochimica Acta* 1992;**195**:163–7.
9. Dash S, Kamruddin M, Ajikumar PK, Tyagi AK, Raj B. Nano-crystalline and metastable phase formation in vacuum thermal decomposition of calcium carbonate. *Thermochimica Acta* 2000;**363**:129–35.
10. Beruto DT, Searcy AW, Mun Gyu Kim. Microstructure, kinetic, thermodynamic analysis for calcite decomposition: free surface and powder bed experiments. *Thermochimica Acta* 2004;**424**:99–109.
11. Rodriguez-Navarro C, Ruiz-Agudo E, Luque A, Rodriguez-Navarro AB, Ortega-Huertas M. Thermal decomposition of calcite: mechanism of formation and textural evolution of CaO nanocrystals. *American Mineralogist* 2009;**94**:578–93.
12. Beruto DT, Erwing J, Searcy AW. The nature of CaO produced by calcite powders decomposition in vacuum and in CO_2. *Journal of the American Ceramic Society* 1979;**62**:580.
13. Beruto DT, Searcy AW, Botter R. The thermodynamics and kinetics of carbon dioxide chemisorption on calcium. *Journal of Physical Chemistry* 1984:88.
14. Beruto DT, Searcy AW, Botter R, Giordani M. Thermodynamics and kinetics of H_2O (V) chemisorption and solubility in nanometric and single-crystal MgO particles during sintering. *Journal of Physical Chemistry* 1993;**97**:9201.
15. Beruto D, Erwing J, Searcy AW. The effect of CO_2 pressure on the rate of decomposition of $CaCO_3$ powders. *Lawrence Berkeley Laboratory* 1979;**78**:112.
16. Beruto DT, Knudsen GF, Searcy AW. Catalysis of the hot pressing of calcium oxide by carbon dioxide gas. In: *American Ceramic Society Meeting*. 1978.
17. Friedman GM. Terminology of crystallization textures and fabrics in sedimentary rocks. *Journal of Sedimentary Research* 1965;**35**:643–55.
18. Rosenholtz JL, Smith DT. Linear thermal expansion of calcite, var, Iceland spar, and Yule marble. *American Mineralogist* 1949;**34**:846–54.
19. DIN EN 459-2, Festlegung, Eigenschaften, Herstellung und Konformität, 2002-01.
20. Meier A, Bonaldi E, Cella GM, Lipinski W, Wuillemin D, Palumbo R. Design and experimental investigation of a horizontal rotary reactor for the solar thermal production of lime. *Energy* 2004;**29**:811–21.
21. Flügel E. *Microfacies of carbonate rocks. Analysis, interpretation and applications*. Springer; 2004, ISBN 3-540-22016-X.
22. Li MQ, Messing GL. Fluoride salt effects on the decomposition of dolomite. *Thermochimica Acta* 1984;**78**(1–3):9–16.
23. Li MQ, Messing GL. Chloride salt effects on the decomposition of dolomite. *Thermochimica Acta* 1983;**68**(1):1–8.
24. Bamford CH, Tipper CFH. *Comprehensive chemical kinetics*, vol. 22. Elsevier; 1980.
25. Burnham AK. Computational aspects of kinetic analysis. Part D: the ICTAC kinetics project – multi-thermal-history model-fitting methods and their relation to isoconversional methods. *Thermochimica Acta* 2000;**355**:165–70.
26. Nishida H, Yamashita M, Hattori N, Endo T, Tokiwa Y. Thermal decomposition of poly(1,4-dioxan-2-one). *Polymer Degradation and Stability* 2000;**70**:485–96.
27. Vyazovkin S, Wight CA. Model-free and model-fitting approaches to kinetic analysis of isothermal and nonisothermal data. *Thermochimica Acta* 1999;**340–341**:53–68.
28. Friedmann JH. *Journal of Polymer Science* 1964–1965;**c6**:183.
29. Vyazovkin S, Clawson JS, Wight C. Thermal dissociation kinetics of solid and liquid ammonium nitrate. *Chemistry of Materials* 2001;**13**:960.
30. Ortega A. A simple and precise linear integral method for isoconversional data. *Thermochimica Acta* 2008.

31. Jacobs PWM, Tompkins FC. In: Garner WE, editor. *Chemistry of the solid state*, vol. 7. 1955.
32. Young DA. *Decomposition of solids*. Pergamon; 1966.
33. Beruto DT, Capurro M, Botter R. Thermally activated step for densification and creep of high-porosity MgO compacts in the intermediate sintering stage. *Journal of European Ceramic Society* 1999;**19**: 623–8.
34. Rahaman MN, De Jonghe LC, Chu M-Y. Effect of green density on densification and creep during sintering. *Journal of American Ceramic Society* 1991;**74**:514–9.
35. Beruto DT, Searcy AW, Fulrath RM, Basu T. Effects of carbon dioxide and sodium chloride on the sintering of calcium oxide. *Lawrence Berkeley Laboratory* 1977;**76**:101.
36. Beruto DT, Kim MG, Barco L. Effect of Li_2CO_3 on the reaction between CaO and CO_2. *Journal of American Ceramic Society* 1984;**67**:274.
37. Conyers, Herring. Surface tension as a motivation for sintering. In: Kingston Walter E, editor. *Symposium on the physics of powder metallurgy*. New York: McGraw-Hill; 1951. p. 143–78.
38. Ravi D, Green DJ. Sintering stresses and distortion produced by density differences in bi-layer structures. *Journal of the European Ceramic Society* 2006;**26**(1–2):17–25.
39. Beruto DT, Guarro S. Kinetic model for dissolution processes of powders in liquid phases. *Materials Chemistry* 1979;**4**:31.
40. IUPAC. Manual of symbols and terminology, appendix 2, part 1. *Colloid and surface chemistry*, vol. 31. International Union of Pure and Applied Chemistry; 1972. p. 0578.